

Spectrum of $J^{PC} = 0^{\pm\pm}$ Gluonic Hidden-Charm Tetraquark States

Bing-Dong Wan^{1,2*}, Ming-Yang Yuan^{1,2}, Jun-Hao Zhang^{1,2}, and Yan Zhang^{1,2}

¹*Department of Physics, Liaoning Normal University, Dalian 116029, China*

²*Center for Theoretical and Experimental High Energy Physics,
Liaoning Normal University, Dalian 116029, China*

Abstract

We investigate gluonic hidden-charm tetraquark states composed of two valence quarks, two valence antiquarks and an explicit valence gluon. In the color configuration $[\bar{3}_c]_{cq} \otimes [8_c]_G \otimes [3_c]_{\bar{c}\bar{q}}$, a complete set of eight interpolating currents is constructed for states with quantum numbers $J^{PC} = 0^{++}, 0^{-+}, 0^{--}$, and 0^{+-} . The corresponding mass spectra are systematically analysed within the QCD sum rule framework, including nonperturbative condensate contributions up to dimension eight. Our numerical analysis indicates the possible existence of six gluonic hidden-charm tetraquark states exhibiting stable behaviour in the adopted Borel windows. By replacing the charm quark with the bottom quark, masses for the corresponding hidden-bottom partners are also estimated. Possible production mechanisms and dominant decay channels are discussed, providing phenomenological guidance for experimental searches. These predicted states may be accessible at current and forthcoming facilities, including Belle II, PANDA, SuperB and LHCb, and thus offer an opportunity to probe explicit gluonic degrees of freedom in multi-quark systems and deepen our understanding of nonperturbative QCD.

* wanbd@lnnu.edu.cn

I. INTRODUCTION

Quantum Chromodynamics (QCD) [1–3] is established as the fundamental theory of the strong interaction. It is generally understood that the essential properties of hadrons are governed by the non-perturbative dynamics of QCD. While perturbation theory provides a robust and well-tested description at high energies, controlled and systematic methods for addressing non-perturbative effects remain limited. Consequently, elucidating the non-perturbative sector of QCD continues to represent a central challenge in modern high-energy physics. In this context, a variety of phenomenological and non-perturbative approaches have been developed and widely employed to investigate hadronic observables, including mass spectra, transition amplitudes, parton distribution functions, and fragmentation functions.

Within the framework of QCD and the quark model (QM) [4, 5], hadronic configurations extending beyond the conventional mesons ($q\bar{q}$) and baryons (qqq) are in principle allowed. Such configurations, commonly referred to as unconventional or exotic hadronic states, include multi-quark states, glueballs, and hybrid mesons. The investigation of these novel structures not only enlarges the hadronic spectrum but also provides a unique window into the underlying dynamics of QCD, particularly in its non-perturbative regime.

Since the beginning of the 21st century, remarkable progress in experimental facilities and analysis techniques in high-energy physics has led to the observation of a growing number of unconventional hadronic states, exemplified by the so-called XYZ states [6–10]. To date, more than forty such states or candidates have been reported, evoking a situation reminiscent of the “particle zoo” era of the last century. It is widely anticipated that many more novel hadronic structures will be discovered in the near future, signaling a renewed era of exploration in hadron spectroscopy. Elucidating the internal structure and dynamical origin of these newly observed states therefore constitutes one of the most compelling and timely challenges in contemporary hadron physics.

Motivated by the experimental successes in the exploration of the XYZ and P_c states, systematic searches for hybrid mesons in the charmonium and bottomonium sectors have been proposed and actively pursued [11–14]. In general, a hybrid state is characterized by a constituent quark–antiquark pair accompanied by an explicit excitation of the gluonic degree

of freedom. The identification and study of such states have become key objectives of several major experimental programs, including BESIII, GlueX, PANDA, and LHCb.

Although hybrid mesons have not yet been unambiguously established experimentally, a number of promising candidates have been reported in recent years as well as in earlier experiments. In particular, the BESIII Collaboration has recently observed a structure with quantum numbers $J^{PC} = 1^{-+}$ at a mass around 1.855 GeV, denoted as $\eta_1(1855)$, in the $\eta\eta'$ invariant mass distribution, with a statistical significance of 19σ [15, 16]. Furthermore, three additional experimental candidates carrying the exotic quantum numbers $I^G J^{PC} = 1^{-}1^{-+}$ have been reported in the past, namely $\pi_1(1400)$ [17], $\pi_1(1600)$ [18, 19] and $\pi_1(2015)$ [20].

Compared with conventional hybrid configurations, a novel class of exotic hybrid states composed of two valence quarks, two valence antiquarks, and a valence gluon has been proposed as a possible interpretation of some unusual features associated with the $X(6900)$ structure [21].

The narrow structure $X(6900)$ was first reported by the LHCb Collaboration in 2020 as a pronounced enhancement in the di- J/ψ invariant mass spectrum around 6.9 GeV. This observation was achieved with a statistical significance exceeding 5σ in proton–proton collisions at center-of-mass energies of $\sqrt{s} = 7, 8, \text{ and } 13$ TeV [22]. It represented the first clear experimental evidence for a distinct structure in the J/ψ -pair mass spectrum, thereby opening a new window for exploring multi-quark dynamics and exotic hadronic configurations.

In 2023, the existence of the $X(6900)$ structure was further corroborated by the CMS Collaboration, which also reported two additional enhancements, denoted as $X(6600)$ and $X(7100)$ [23]. Notably, the mass of $X(6900)$ lies approximately 700 MeV above the double- J/ψ threshold, which is significantly larger than the typical mass splittings observed between ground and excited states in conventional quarkonium systems. Within the tetraquark hybrid framework, such a large energy separation can be naturally attributed to the presence of an excited gluonic degree of freedom. In this context, the emergence of a higher-mass structure such as $X(7100)$ is also anticipated.

In analogy with the proposed tetracharm hybrid configuration, one may also construct a class of gluonic charmonium-like states in which a charm–anticharm pair is partially replaced

by a light quark pair, e.g., an up quark and an anti-down quark. In this scenario, the diquark pairs cq and $\bar{c}\bar{q}$ are arranged in the color $\bar{\mathbf{3}}_c$ and $\mathbf{3}_c$ representations, respectively, within the $SU(3)_c$ gauge group. Together with a dynamical gluon in the color octet representation, the resulting configuration of such gluonic charmonium-like states can be expressed as

$$[\bar{\mathbf{3}}_c]_{cq} \otimes [\mathbf{8}_c]_G \otimes [\mathbf{3}_c]_{\bar{c}\bar{q}}. \quad (1)$$

In our previous work [24], tetraquark hybrid states with quantum numbers $J^P = 0^-, 1^-, 0^+, 1^+$ were studied. Owing to the increased complexity of the interpolating currents and the associated computational difficulties, the C -parity was not considered. In this paper, we investigate the $0^{\pm\pm}$ gluonic charmonium-like states within the framework of QCD sum rules (QCDSR) [25]. Unlike phenomenological models, QCDSR is a first-principle, QCD-based nonperturbative approach that systematically incorporates vacuum condensates through the operator product expansion, thereby providing a self-consistent description of hadronic properties governed by nonperturbative QCD dynamics. Over the past decades, this method has achieved remarkable success in the study of hadron spectroscopy and exotic states [24–55].

To formulate the QCD sum rules, the first step is to construct appropriate interpolating currents that carry the same quantum numbers as the hadron of interest. Using these currents, one then defines the two-point correlation function, which admits two distinct representations: a QCD (theoretical) side, evaluated via the operator product expansion, and a phenomenological (hadronic) side, expressed in terms of physical intermediate states. By matching these two representations through a dispersion relation and applying a Borel transformation, the sum rule is established, from which the hadron mass can be extracted in a systematic manner.

The rest of this paper is organized as follows. In Sec. II, we present a brief overview of the QCD sum rule method together with the essential formulas used in our analysis. The numerical results and discussions are given in Sec. III. Possible production mechanisms and decay modes of the hybrid states are discussed in Sec. IV. Finally, a brief summary is presented in the last section.

II. FORMALISM

In the QCD sum rule framework, the two-point correlation function is defined as

$$\Pi(q^2) = i \int d^4x e^{iq \cdot x} \langle 0 | T \{ j(x), j^\dagger(0) \} | 0 \rangle. \quad (2)$$

To evaluate the mass spectrum of gluonic tetraquark states, the corresponding interpolating currents are constructed [21]. For the 0^{++} state, the currents take the forms:

$$j_{0^{++}}^A(x) = g_s \epsilon_{ikl} \epsilon_{jmn} [q_k^T C \gamma_\mu c_l] \frac{\lambda_{ij}^a}{2} G_{\mu\nu}^a [\bar{q}_m \gamma_\nu C \bar{c}_n^T], \quad (3)$$

$$j_{0^{++}}^B(x) = g_s \epsilon_{ikl} \epsilon_{jmn} [q_k^T C \gamma_\mu \gamma_5 c_l] \frac{\lambda_{ij}^a}{2} G_{\mu\nu}^a [\bar{q}_m \gamma_\nu \gamma_5 C \bar{c}_n^T], \quad (4)$$

$$j_{0^{++}}^C(x) = \frac{g_s \epsilon_{ikl} \epsilon_{jmn}}{\sqrt{2}} \left\{ [q_k^T C \gamma_\mu c_l] \frac{\lambda_{ij}^a}{2} \tilde{G}_{\mu\nu}^a [\bar{c}_m \gamma_\nu \gamma_5 C \bar{q}_n^T] \right. \\ \left. + [q_k^T C \gamma_\mu \gamma_5 c_l] \frac{\lambda_{ij}^a}{2} \tilde{G}_{\mu\nu}^a [\bar{c}_m \gamma_\nu C \bar{q}_n^T] \right\}. \quad (5)$$

Here, q denotes the up or down quarks; $G_{\mu\nu}^a$ and $\tilde{G}_{\mu\nu}^a$ represent the gluon field strength tensor and its dual, with $\tilde{G}_{\mu\nu}^a = \frac{1}{2} \epsilon_{\mu\nu\alpha\beta} G^{a;\alpha\beta}$; g_s is the QCD coupling constant; λ^a are the Gell-Mann matrices; C denotes the charge conjugation matrix; and i, j, k, \dots are color indices.

For the 0^{-+} state, the interpolating currents are:

$$j_{0^{-+}}^A(x) = g_s \epsilon_{ikl} \epsilon_{jmn} [q_k^T C \gamma_\mu c_l] \frac{\lambda_{ij}^a}{2} \tilde{G}_{\mu\nu}^a [\bar{q}_m \gamma_\nu C \bar{c}_n^T], \quad (6)$$

$$j_{0^{-+}}^B(x) = g_s \epsilon_{ikl} \epsilon_{jmn} [q_k^T C \gamma_\mu \gamma_5 c_l] \frac{\lambda_{ij}^a}{2} \tilde{G}_{\mu\nu}^a [\bar{q}_m \gamma_\nu \gamma_5 C \bar{c}_n^T], \quad (7)$$

$$j_{0^{-+}}^C(x) = \frac{g_s \epsilon_{ikl} \epsilon_{jmn}}{\sqrt{2}} \left\{ [q_k^T C \gamma_\mu c_l] \frac{\lambda_{ij}^a}{2} G_{\mu\nu}^a [\bar{q}_m \gamma_\nu \gamma_5 C \bar{c}_n^T] \right. \\ \left. + [q_k^T C \gamma_\mu c_l] \frac{\lambda_{ij}^a}{2} G_{\mu\nu}^a [\bar{q}_m \gamma_\nu \gamma_5 C \bar{c}_n^T] \right\}. \quad (8)$$

For the 0^{--} and 0^{+-} states, the currents are:

$$j_{0^{--}}^A(x) = \frac{g_s \epsilon_{ikl} \epsilon_{jmn}}{\sqrt{2}} \left\{ [q_k^T C \gamma_\mu c_l] \frac{\lambda_{ij}^a}{2} G_{\mu\nu}^a [\bar{q}_m \gamma_\nu \gamma_5 C \bar{c}_n^T] \right. \\ \left. - [q_k^T C \gamma_\mu c_l] \frac{\lambda_{ij}^a}{2} G_{\mu\nu}^a [\bar{q}_m \gamma_\nu \gamma_5 C \bar{c}_n^T] \right\}, \quad (9)$$

$$j_{0^{+-}}^A(x) = \frac{g_s \epsilon_{ikl} \epsilon_{jmn}}{\sqrt{2}} \left\{ [q_k^T C \gamma_\mu c_l] \frac{\lambda_{ij}^a}{2} \tilde{G}_{\mu\nu}^a [\bar{c}_m \gamma_\nu \gamma_5 C \bar{q}_n^T] \right. \\ \left. - [q_k^T C \gamma_\mu \gamma_5 c_l] \frac{\lambda_{ij}^a}{2} \tilde{G}_{\mu\nu}^a [\bar{c}_m \gamma_\nu C \bar{q}_n^T] \right\}. \quad (10)$$

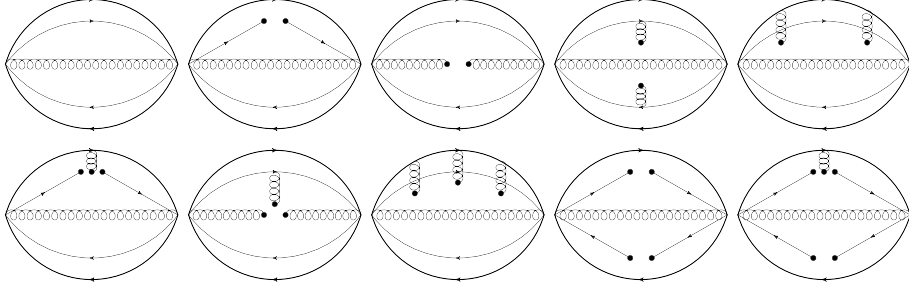


FIG. 1: The typical Feynman diagrams associated with the correlation function are shown, where the thick solid line represents the heavy quark, the thin solid line denotes the light quark, and the wavy line corresponds to the gluon.

On the OPE side, the correlation function can be expressed as

$$\Pi^{OPE}(q^2) = \int_{s_{min}}^{\infty} ds \frac{\rho^{OPE}(s)}{s - q^2}, \quad (11)$$

where $\rho^{OPE}(s) = \text{Im}[\Pi^{OPE}(s)]/\pi$ is the spectral density, and $s_{min} = (2m_c + 2m_q)^2$. Up to dimension-eight condensates, it reads

$$\rho^{OPE}(s) = \rho^{pert}(s) + \rho^{\langle \bar{q}q \rangle}(s) + \rho^{\langle G^2 \rangle}(s) + \rho^{\langle \bar{q}Gq \rangle}(s) + \rho^{\langle \bar{q}q \rangle^2}(s) + \rho^{\langle G^3 \rangle}(s) + \rho^{\langle \bar{q}q \rangle \langle \bar{q}Gq \rangle}(s). \quad (12)$$

The Feynman diagrams corresponding to these contributions are illustrated in Fig. 1, where the thick solid line represents the heavy quark, the thin solid line denotes the light quark, and the wavy line corresponds to the gluon. Each diagram provides a visual representation of how different condensates and perturbative contributions enter the correlation function, with lower-dimensional condensates typically associated with simpler topologies and higher-dimensional condensates corresponding to more complex gluon insertions or multi-quark interactions.

On the phenomenological side, the correlation function is written as

$$\Pi^{phen}(q^2) = \frac{\lambda^2}{m^2 - q^2} + \frac{1}{\pi} \int_{s_0}^{\infty} ds \frac{\rho(s)}{s - q^2}, \quad (13)$$

where m , λ , $\rho(s)$, and s_0 denote the hadron mass, coupling constant, spectral density of higher states, and continuum threshold.

To suppress contributions from higher-dimensional condensates and continuum states, a

Borel transformation is applied:

$$\hat{B}[f(Q^2)] := \lim_{\substack{Q^2 \rightarrow \infty, n \rightarrow \infty \\ Q^2/n = M_B^2}} \frac{(-Q^2)^n}{(n-1)!} \left(\frac{d}{dQ^2} \right)^n f(Q^2). \quad (14)$$

After the Borel transformation and applying quark–hadron duality, the QCD sum rule reads

$$\lambda^2 e^{-m^2/M_B^2} + \int_{s_0}^{\infty} ds \rho^{OPE}(s) e^{-s/M_B^2} = \int_{s_{min}}^{\infty} ds \rho^{OPE}(s) e^{-s/M_B^2}, \quad (15)$$

from which the tetraquark mass is extracted as

$$m(s_0, M_B^2) = \sqrt{-\frac{L_1(s_0, M_B^2)}{L_0(s_0, M_B^2)}}, \quad (16)$$

with

$$L_0(s_0, M_B^2) = \int_{s_{min}}^{s_0} ds \rho(s) e^{-s/M_B^2}, \quad (17)$$

$$L_1(s_0, M_B^2) = \frac{\partial}{\partial \frac{1}{M_B^2}} L_0(s_0, M_B^2). \quad (18)$$

III. NUMERICAL ANALYSIS

To perform numerical evaluations, the following widely adopted input parameters are used [25, 26, 29–31]:

$$\begin{aligned} m_c(m_c) &= \bar{m}_c = (1.275 \pm 0.025) \text{ GeV}, & m_b(m_b) &= \bar{m}_b = (4.18 \pm 0.03) \text{ GeV}, \\ m_u &= 2.16_{-0.26}^{+0.49} \text{ MeV}, & m_d &= 4.67_{-0.17}^{+0.48} \text{ MeV}, \\ \langle \bar{q}q \rangle &= -(0.23 \pm 0.03)^3 \text{ GeV}^3, & \langle g_s^2 G^2 \rangle &= 0.88 \text{ GeV}^4, & \langle g_s^3 G^3 \rangle &= 0.045 \text{ GeV}^6, \\ \langle \bar{q}g_s \sigma \cdot Gq \rangle &= m_0^2 \langle \bar{q}q \rangle, & m_0^2 &= (0.8 \pm 0.2) \text{ GeV}^2, \end{aligned} \quad (19)$$

The $\overline{\text{MS}}$ running masses are used for the heavy quarks. The leading-order strong coupling constant is taken as

$$\alpha_s(M_B^2) = \frac{4\pi}{\left(11 - \frac{2}{3}n_f\right) \ln\left(\frac{M_B^2}{\Lambda_{\text{QCD}}^2}\right)}, \quad (20)$$

with $\Lambda_{\text{QCD}} = 300 \text{ MeV}$ and n_f being the number of active quark flavors.

Moreover, the extracted masses of the tetraquark hybrid states depend explicitly on the continuum threshold s_0 and the Borel parameter M_B^2 . The introduction of these two auxiliary parameters in the establishment of the sum rules must satisfy two essential criteria [25, 26, 29, 30]. The first requirement concerns the convergence of the operator product expansion. In order to provide a reliable description of the ground-state contribution within a truncated OPE, the contributions from higher-dimensional condensates should be sufficiently suppressed, so that uncertainties resulting from neglected higher-order terms remain under control. In practice, this is ensured by examining the relative weight of higher-dimensional condensates compared to the total OPE contribution, and then selecting an appropriate Borel window for M_B^2 in which the OPE exhibits good convergence. The convergence condition of the OPE can be expressed as

$$R^{OPE} = \left| \frac{L_0^{dim=8}(s_0, M_B^2)}{L_0(s_0, M_B^2)} \right|, \quad (21)$$

The second requirement is that the pole contribution (PC) must be sufficiently large to ensure that the extracted mass is dominated by the ground-state resonance rather than by excited or continuum states. In practical analyses, a reliable sum rule extraction typically requires the pole contribution to be larger than 40% of the total dispersion integral [32]. The pole contribution is defined as

$$R^{PC} = \frac{L_0(s_0, M_B^2)}{L_0(\infty, M_B^2)}. \quad (22)$$

Furthermore, among the values of s_0 that satisfy the above two criteria, one must determine the optimal choice that yields a reliable Borel window for the parameter M_B^2 . It should be emphasized that M_B^2 is not a physical observable. Therefore, within the working Borel window corresponding to a given s_0 , the extracted hadron mass should exhibit minimal dependence on M_B^2 . In practical calculations, the continuum threshold is varied in steps of 0.2 GeV to fix its central value and to estimate the associated uncertainties [33, 34]. This procedure determines both the optimal range of s_0 and the corresponding uncertainty of the predicted mass.

With the above preparations, we are now in a position to numerically evaluate the mass spectrum of the tetraquark hybrid states. As an illustrative example, the ratios $R_{0^{++}}^{B, OPE}$ and $R_{0^{++}}^{B, PC}$ associated with the current in Eq. (4) are displayed in Fig. 2(a) as functions of the

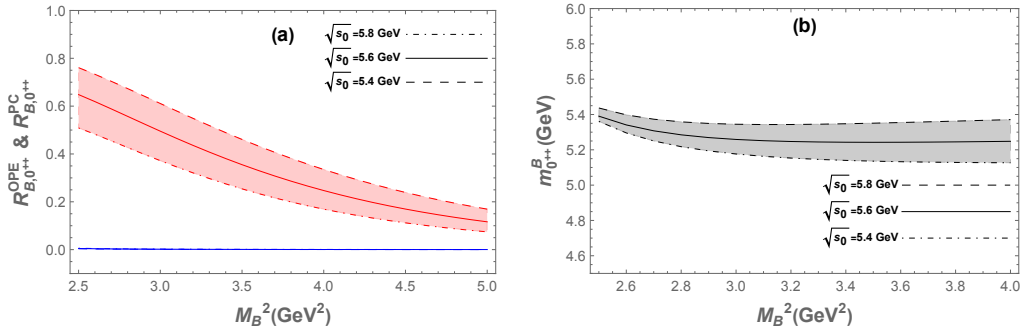


FIG. 2: (a) The ratios $R_{0^{++}}^{B, OPE}$ and $R_{0^{++}}^{B, PC}$ as functions of the Borel parameter M_B^2 for different values of $\sqrt{s_0}$, where blue lines represent $R_{0^{++}}^{B, OPE}$ and red lines denote $R_{0^{++}}^{B, PC}$. (b) The mass $M_{0^{++}}^B$ as a function of the Borel parameter M_B^2 for different values of $\sqrt{s_0}$.

Borel parameter M_B^2 for different values of the continuum threshold, namely $\sqrt{s_0} = 5.4, 5.6,$ and 5.8 GeV. The corresponding dependence of $m_{0^{++}}^B$ on M_B^2 is shown in Fig. 2(b). The optimal Borel window is determined to be $2.6 \leq M_B^2 \leq 3.4$ GeV² within which a smooth and stable plateau emerges in the $m_{0^{++}}^B - M_B^2$ curve. This behavior signals the reliability of the extracted mass for the possible 0^{++} tetraquark hybrid state. Accordingly, the mass $m_{0^{++}}^B$ is obtained as

$$m_{0^{++}}^B = (5.24 \pm 0.10) \text{ GeV} . \quad (23)$$

Following the same procedure, the OPE convergence, pole contribution, and the dependence of the extracted masses on the Borel parameter M_B^2 are presented in Appendix B. The resulting mass values are then obtained and collected in Table I. For the currents in Eqs. (3) and (6), however, no appropriate Borel window can be identified in which the masses exhibit sufficient stability with respect to variations of M_B^2 . This suggests that these currents have no strong coupling to hidden-charm tetraquark hybrid states.

For the bottom sector, performing the same procedure but with m_c replaced by m_b , readers can find the OPE, pole contribution and the masses as functions of Borel parameter M_B^2 in the Appendix B, we can easily obtain the masses of the hidden-bottom tetraquark hybrid states. The relevant numerical results are tabulated in Table II

The uncertainties quoted in Tables I and II are mainly induced by the variations of the input parameters, including the quark masses, the condensates, and the continuum threshold

TABLE I: The continuum thresholds, Borel parameters, and predicted masses of the hidden-charm tetraquark hybrid states.

J^P	Current	$\sqrt{s_0}$ (GeV)	M_B^2 (GeV 2)	M^X (GeV)
0^{++}	A	–	–	–
	B	5.6 ± 0.2	$2.6 - 3.4$	5.24 ± 0.10
	C	5.7 ± 0.2	$2.6 - 3.3$	5.33 ± 0.10
0^{-+}	A	–	–	–
	B	5.7 ± 0.2	$2.6 - 3.5$	5.32 ± 0.12
	C	5.9 ± 0.2	$2.6 - 3.7$	5.46 ± 0.12
0^{--}	A	5.8 ± 0.2	$2.6 - 3.9$	5.40 ± 0.13
0^{+-}	A	5.6 ± 0.2	$2.6 - 3.5$	5.28 ± 0.12

TABLE II: The continuum thresholds, Borel parameters, and predicted masses of the hidden-bottom tetraquark hybrid states.

J^P	Current	$\sqrt{s_0}$ (GeV)	M_B^2 (GeV 2)	M^X (GeV)
0^{++}	A	–	–	–
	B	11.6 ± 0.2	$6.3 - 7.6$	11.15 ± 0.11
	C	11.7 ± 0.2	$6.2 - 7.4$	11.23 ± 0.11
0^{-+}	A	–	–	–
	B	11.7 ± 0.2	$6.5 - 7.9$	11.22 ± 0.11
	C	11.8 ± 0.2	$6.5 - 7.7$	11.29 ± 0.11
0^{--}	A	11.7 ± 0.2	$6.3 - 7.4$	11.23 ± 0.11
0^{+-}	A	11.6 ± 0.2	$6.2 - 7.2$	11.17 ± 0.11

$\sqrt{s_0}$.

IV. PRODUCTION AND DECAY MECHANISMS OF THE $0^{\pm\pm}$ TETRAQUARK-HYBRID STATES

According to our QCD sum rule analysis, the masses of the hidden-charm tetraquark-hybrid states lie in the range $5.14 \text{ GeV} \leq m_X \leq 5.58 \text{ GeV}$. This mass region is above

the open-charm thresholds and overlaps with the energy domain where a variety of exotic charmonium-like structures, commonly referred to as the XYZ states, have been reported. Consequently, the production and decay mechanisms of such tetraquark–hybrid states are expected to be rich and experimentally accessible.

A. Production mechanisms

1. Gluon-dominated production in hadron colliders

Due to the explicit valence gluon in their internal structure, tetraquark–hybrid states can be efficiently produced in gluon-rich environments, such as high-energy proton–proton collisions at the LHC. Typical partonic subprocesses include

$$g + g \rightarrow c\bar{c} + q\bar{q} + g, \quad (24)$$

where the additional gluon becomes an intrinsic constituent of the hybrid configuration. Non-perturbative hadronization of such partonic systems may lead to the formation of compact tetraquark–hybrid states, making LHC and LHCb particularly suitable for searches in invariant mass spectra of charmonium plus light hadrons.

2. Production in e^+e^- annihilation

In the energy region around 5–6 GeV, production via e^+e^- annihilation is influenced by intermediate vector charmonium resonances, e.g.,

$$e^+e^- \rightarrow \psi^* \rightarrow X_{\text{hybrid}} + \pi(\pi/\eta), \quad (25)$$

where X_{hybrid} denotes a hidden-charm tetraquark–hybrid state. Such processes are within the capabilities of Belle II, and SuperKEKB.

3. Production in B -meson decays

Weak decays of B mesons also provide a production mechanism:

$$B \rightarrow X_{\text{hybrid}} + K(\pi), \quad (26)$$

where the underlying quark-level transition $b \rightarrow c\bar{c}s$ naturally produces a hidden-charm pair, and an excited gluon may become part of the hybrid configuration.

B. Decay mechanisms of $0^{\pm\pm}$ states

The decay patterns of tetraquark–hybrid states are governed by their spin-parity-charge conjugation quantum numbers (J^{PC}), mass thresholds, and internal gluonic content. The dominant decay modes can be summarized in Table III.

TABLE III: Dominant decay channels of the $0^{\pm\pm}$ hidden-charm tetraquark–hybrid states. Here, "OC" stands for open-charm meson decays, "HC" for hidden-charm meson decays, "Rad" for radiative decays, and "BB" for baryon–antibaryon decays.

J^{PC}	Decay channels	Type
0^{++}	$D\bar{D}, D^*\bar{D}^*, D_s\bar{D}_s$	OC
	$J/\psi\omega, \eta_c f_0(980), \chi_{c0}\eta$	HC
	$J/\psi\gamma, \chi_{c1}\gamma$	Rad
	$\Lambda_c\bar{\Lambda}_c, \Sigma_c\bar{\Sigma}_c, \Xi_c\bar{\Xi}_c$	BB
0^{--}	$J/\psi\pi^0, J/\psi\eta, D\bar{D}^*(L=1)$	HC/OC
	$J/\psi + \pi^+\pi^-, D\bar{D} + \pi$	Multi-body
	$\Lambda_c\bar{\Lambda}_c, \Sigma_c\bar{\Sigma}_c, \Xi_c\bar{\Xi}_c$	BB
0^{+-}	$J/\psi + \pi + \pi, \eta_c + \rho + \pi$	HC/Multi-body
	$D\bar{D} + \pi, D^*\bar{D} + \pi$	OC/Multi-body
	$\Lambda_c\bar{\Lambda}_c, \Sigma_c\bar{\Sigma}_c, \Xi_c\bar{\Xi}_c$	BB
0^{-+}	$D\bar{D}^*, D^*\bar{D}^*(L=1)$	OC
	$J/\psi\eta, \eta_c\omega$	HC
	$J/\psi\gamma, \eta_c\gamma$	Rad
	$\Lambda_c\bar{\Lambda}_c, \Sigma_c\bar{\Sigma}_c, \Xi_c\bar{\Xi}_c$	BB

It should be noted that the masses of the tetraquark–hybrid states in our calculation are close in magnitude to those of the hidden-charm hexaquarks reported in Refs. [36, 56, 57]. The main difference lies in the decay branching ratios into $\Xi_c \bar{\Xi}_c$ final states. For tetraquark–hybrid states, the branching ratios of $\Xi_c \bar{\Xi}_c$ are comparable to those of $\Sigma_c \bar{\Sigma}_c$, while for hidden-charm hexaquarks, the Cabibbo-Kobayashi-Maskawa suppression renders the $\Xi_c \bar{\Xi}_c$ branching ratios relatively small. This distinction may serve as a phenomenological handle to discriminate between these two types of exotic states in experimental searches.

The multi-body and radiative decay channels, particularly for the exotic 0^{--} and 0^{+-} states, offer distinctive signatures for experimental investigations. Analyses of invariant mass spectra in $D^{(*)} \bar{D}^{(*)}$, $J/\psi \pi \pi$, and $J/\psi \gamma$ channels at Belle II, SuperKEKB, PANDA, and LHCb are expected to be crucial in identifying these tetraquark–hybrid states and probing the role of gluonic excitations in hadron spectroscopy.

V. SUMMARY

In summary, we have studied the hidden-charm and hidden-bottom tetraquark hybrid states with quantum numbers $J^{PC} = 0^{\pm\pm}$, composed of two valence quarks, two valence antiquarks, and an explicit valence gluon. A complete set of eight interpolating currents was constructed with the color configuration

$$[\bar{\mathbf{3}}_c]_{cq} \otimes [\mathbf{8}_c]_G \otimes [\mathbf{3}_c]_{\bar{c}\bar{q}}. \quad (27)$$

Within the framework of QCD sum rules, we systematically evaluated the corresponding mass spectra. Our numerical analysis suggests the possible existence of six hidden-charm and hidden-bottom tetraquark hybrid states, and the resulting mass predictions are summarized in Tabs. I and II for the charm and bottom sectors, respectively.

We further investigated the possible production and decay channels of the hidden-charm tetraquark hybrid states. Since the parent particles involved in these processes can be copiously produced in current experiments, the corresponding tetraquark hybrid states may be accessible at facilities such as BELLE II, PANDA, Super-B, and LHCb.

Special attention has been paid to the states with exotic quantum numbers $J^{PC} = 0^{--}$

and 0^{+-} . While these quantum numbers cannot be realized by conventional $q\bar{q}$ mesons, they may arise from different nonconventional configurations, including three-gluon (ggg) glueballs. Therefore, an assignment based solely on quantum numbers is not sufficient to identify the underlying structure of such states.

In this work, the tetraquark hybrid interpretation can nevertheless be distinguished from the three-gluon glueball scenario in several aspects. The presence of heavy quarks implies a significantly higher mass scale for the hidden-charm and hidden-bottom tetraquark hybrid states compared to the expected masses of light ggg glueballs. Moreover, the color configuration $[\bar{3}_c]_{cq} \otimes [8_c]_G \otimes [3_c]_{\bar{c}\bar{q}}$ corresponds to a diquark–antidiquark core coupled to a valence gluon, leading to characteristic decay patterns involving heavy quarkonium states. In contrast, three-gluon glueballs are expected to couple predominantly to light hadrons, with suppressed decay rates into heavy quarkonium.

In addition, the production mechanisms of these two types of states are expected to be markedly different. Heavy tetraquark hybrid states are favored in processes associated with heavy-flavor production, such as heavy quarkonium decays and high-energy hadronic collisions, whereas three-gluon glueballs are more naturally produced in gluon-rich environments without heavy-flavor enhancement. These differences in mass scales, internal structures, and production and decay properties provide viable experimental criteria for disentangling tetraquark hybrid states from possible glueball candidates.

Finally, the tetraquark hybrid states in the bottom sector are predicted to be significantly heavier than their charm counterparts, rendering their experimental production more challenging. Moreover, one of the proposed production mechanisms proceeds through Υ decays, which is not applicable to the hidden-bottom tetraquark hybrid states themselves. As a consequence, experimental searches for hidden-bottom tetraquark hybrid states are expected to be considerably more difficult than those for the hidden-charm sector.

Acknowledgments

This work was supported in part by the National Natural Science Foundation of China under Grants 12575106 and 12147214, and Specific Fund of Fundamental Scientific Research

- [1] D. J. Gross and F. Wilczek, Phys. Rev. Lett. **30**, 1343 (1973).
- [2] H. D. Politzer, Phys. Rev. Lett. **30**, 1346 (1973).
- [3] K. G. Wilson, Phys. Rev. D **10**, 2445 (1974).
- [4] M. Gell-Mann, Phys. Lett. **8**, 214 (1964).
- [5] G. Zweig, Report No. CERN-TH-401.
- [6] S. K. Choi *et al.* [Belle Collaboration], Phys. Rev. Lett. **91**, 262001 (2003).
- [7] B. Aubert *et al.* [BaBar Collaboration], Phys. Rev. Lett. **95**, 142001 (2005).
- [8] A. Bondar *et al.* [Belle Collaboration], Phys. Rev. Lett. **108**, 122001 (2012).
- [9] M. Ablikim *et al.* [BESIII Collaboration], Phys. Rev. Lett. **110**, 252001 (2013).
- [10] Z. Q. Liu *et al.* [Belle Collaboration], Phys. Rev. Lett. **110**, 252002 (2013).
- [11] S. L. Olsen, Nucl. Phys. A **827**, 53C-60C (2009).
- [12] S. L. Olsen, [arXiv:0909.2713 [hep-ex]].
- [13] S. Godfrey and S. L. Olsen, Ann. Rev. Nucl. Part. Sci. **58**, 51-73 (2008).
- [14] F. E. Close, eConf **C070512**, 020 (2007).
- [15] M. Ablikim *et al.* [BESIII], Phys. Rev. Lett. **129**, 192002 (2022) [erratum: Phys. Rev. Lett. **130**, 159901 (2023)].
- [16] M. Ablikim *et al.* [BESIII], Phys. Rev. D **106**, 072012 (2022) [erratum: Phys. Rev. D **107**, 079901 (2023)].
- [17] D. Alde *et al.* [IHEP-Brussels-Los Alamos-Annecey(LAPP)], Phys. Lett. B **205**, 397 (1988).
- [18] E. I. Ivanov *et al.* [E852], Phys. Rev. Lett. **86**, 3977-3980 (2001).
- [19] M. Alekseev *et al.* [COMPASS], Phys. Rev. Lett. **104**, 241803 (2010).
- [20] J. Kuhn *et al.* [E852], Phys. Lett. B **595**, 109-117 (2004).
- [21] B. D. Wan and C. F. Qiao, Phys. Lett. B **817**, 136339 (2021).
- [22] R. Aaij *et al.* [LHCb], Sci. Bull. **65**, 1983 (2020).
- [23] A. Hayrapetyan *et al.* [CMS], Phys. Rev. Lett. **132**, 111901 (2024).
- [24] B. D. Wan and S. Yang, Eur. Phys. J. A **61**, 11 (2025).
- [25] M.A. Shifman, A.I. Vainshtein and V.I. Zakharov, Nucl. Phys. B**147**, 385 (1979); *ibid.*, Nucl. Phys. B**147**, 448 (1979).
- [26] R. M. Albuquerque, arXiv:1306.4671 [hep-ph].
- [27] Z. G. Wang and T. Huang, Phys. Rev. D **89**, 054019 (2014).

- [28] J. Govaerts, L. J. Reinders, H. R. Rubinstein and J. Weyers, Nucl. Phys. B **258**, 215-229 (1985).
- [29] L. J. Reinders, H. Rubinstein and S. Yazaki, Phys. Rept. **127**, 1 (1985).
- [30] P. Colangelo and A. Khodjamirian, in *At the frontier of particle physics / Handbook of QCD*, edited by M. Shifman (World Scientific, Singapore, 2001), arXiv:hep-ph/0010175.
- [31] S. Narison, World Sci. Lect. Notes Phys. **26** 1 (1989).
- [32] C. M. Tang, Y. C. Zhao and L. Tang, Phys. Rev. D **105**, 114004 (2022).
- [33] C. F. Qiao and L. Tang, Phys. Rev. Lett. **113**, 221601 (2014).
- [34] L. Tang and C. F. Qiao, Nucl. Phys. B **904**, 282 (2016).
- [35] L. Tang, B. D. Wan, K. Maltman and C. F. Qiao, Phys. Rev. D **101**, 094032 (2020).
- [36] B. D. Wan, L. Tang and C. F. Qiao, Eur. Phys. J. C **80**, 121 (2020).
- [37] C. M. Tang, C. G. Duan and L. Tang, [arXiv:2405.05042 [hep-ph]].
- [38] B. D. Wan and C. F. Qiao, Nucl. Phys. B **968**, 115450 (2021).
- [39] S. N. Li and L. Tang, [arXiv:2404.11145 [hep-ph]].
- [40] B. D. Wan, S. Q. Zhang and C. F. Qiao, Phys. Rev. D **105**, 014016 (2022).
- [41] Y. C. Zhao, C. M. Tang and L. Tang, Eur. Phys. J. C **83**, 654 (2023).
- [42] B. D. Wan, S. Q. Zhang and C. F. Qiao, Phys. Rev. D **106**, 074003 (2022).
- [43] S. Q. Zhang, B. D. Wan, L. Tang and C. F. Qiao, Phys. Rev. D **106**, 074010 (2022).
- [44] B. D. Wan and C. F. Qiao, [arXiv:2208.14042 [hep-ph]].
- [45] F. H. Yin, W. Y. Tian, L. Tang and Z. H. Guo, Eur. Phys. J. C **81**, 818 (2021).
- [46] B. D. Wan, Eur. Phys. J. C **84**, 760 (2024).
- [47] B. C. Yang, L. Tang and C. F. Qiao, Eur. Phys. J. C **81**, 324 (2021).
- [48] B. D. Wan, Nucl. Phys. B **1004**, 116538 (2024).
- [49] B. D. Wan and H. T. Xu, Chin. Phys. C **44**, 093105 (2024).
- [50] B. D. Wan and Y. R. Wang, Eur. Phys. J. A **60**, 179 (2024).
- [51] B. D. Wan and J. C. Yang, [arXiv:2507.11874 [hep-ph]].
- [52] B. D. Wan, [arXiv:2508.07822 [hep-ph]].
- [53] B. D. Wan, J. H. Zhang and Y. Zhang, [arXiv:2508.10763 [hep-ph]].
- [54] B. D. Wan, Eur. Phys. J. Plus **140**, 873 (2025).
- [55] B. D. Wan, Y. Zhang, J. H. Zhang and M. Y. Yuan, [arXiv:2512.03800 [hep-ph]].
- [56] X. W. Wang, Z. G. Wang and G. I. Yu, Eur. Phys. J. A **57**, 275 (2021).
- [57] Z. Liu, H. T. An, Z. W. Liu and X. Liu, Phys. Rev. D **105**, 034006 (2022).

Appendix A: The spectral densities for gluonic tetraquark states

1. The spectral densities for 0^{++} gluonic tetraquark states

For the current shown in Eq. (3), we obtain the spectral densities as follows:

$$\rho_{0^{++},A}^{pert}(s) = \int_{\alpha_{min}}^{\alpha_{max}} d\alpha \int_{\beta_{min}}^{1-\alpha} d\beta \frac{g_s^2 \mathcal{F}_{\alpha\beta}^5 (\alpha + \beta - 1)^3 (\mathcal{F}_{\alpha\beta} + 3m_c m_q (\alpha + \beta))}{5 \times 3^2 \times 2^{11} \pi^8 \alpha^5 \beta^5}, \quad (A1)$$

$$\begin{aligned} \rho_{0^{++},A}^{\langle \bar{q}q \rangle}(s) &= \frac{\langle \bar{q}q \rangle}{\pi^6} \int_{\alpha_{min}}^{\alpha_{max}} d\alpha \int_{\beta_{min}}^{1-\alpha} d\beta \frac{g_s^2 \mathcal{F}_{\alpha\beta}^3 (\alpha + \beta - 1)}{3 \times 2^9 \alpha^4 \beta^4} (4\alpha\beta \mathcal{F}_{\alpha\beta} m_q \\ &+ 4\alpha\beta m_c m_q^2 (\alpha + \beta) - m_c \mathcal{F}_{\alpha\beta} (\alpha + \beta) (\alpha + \beta - 1)), \end{aligned} \quad (A2)$$

$$\begin{aligned} \rho_{0^{++},A}^{\langle G^2 \rangle, I}(s) &= \frac{\langle g_s^2 G^2 \rangle}{\pi^6} \int_{\alpha_{min}}^{\alpha_{max}} d\alpha \int_{\beta_{min}}^{1-\alpha} d\beta \frac{m_c \mathcal{F}_{\alpha\beta}^2 (\alpha + \beta - 1)}{3 \times 2^9 \alpha^3 \beta^3} (\mathcal{F}_{\alpha\beta} m_q (\alpha \\ &+ \beta) + 6\alpha\beta m_c m_q^2), \end{aligned} \quad (A3)$$

$$\begin{aligned} \rho_{0^{++},A}^{\langle G^2 \rangle, II}(s) &= \frac{g_s^2 \langle g_s^2 G^2 \rangle}{\pi^8} \int_{\alpha_{min}}^{\alpha_{max}} d\alpha \int_{\beta_{min}}^{1-\alpha} d\beta \left(\frac{m_c \mathcal{F}_{\alpha\beta}^2 (\alpha + \beta - 1)^3}{3^3 \times 2^{12} \alpha^5 \beta^5} (\alpha^3 \mathcal{F}_{\alpha\beta} (2m_c + 3m_q) \right. \\ &+ \beta^3 \mathcal{F}_{\alpha\beta} (2m_c + 3m_q) + 3m_q m_c^2 (\alpha^3 + \beta^3) (\alpha + \beta)) + \frac{\mathcal{F}_{\alpha\beta}^3 (\alpha + \beta - 1)}{3^3 \times 2^{19} \alpha^4 \beta^4} \\ &\times (\mathcal{F}_{\alpha\beta} (1 - 5\alpha + 4\alpha^2 - 5\beta + 4\beta^2 + 14\alpha\beta) + 4m_c (\alpha + \beta - 1) (\beta m_q (49\alpha + 4\beta \\ &- 1) + \alpha m_q (49\beta + 4\alpha - 1))) \left. \right), \end{aligned} \quad (A4)$$

$$\begin{aligned} \rho_{0^{++},A}^{\langle \bar{q}Gq \rangle}(s) &= \frac{\langle g_s \bar{q} \sigma \cdot Gq \rangle}{\pi^6} \int_{\alpha_{min}}^{\alpha_{max}} d\alpha \int_{\beta_{min}}^{1-\alpha} d\beta \frac{g_s^2 \mathcal{F}_{\alpha\beta}^2}{3^2 \times 2^{13} \alpha^3 \beta^3} (-128\alpha\beta \mathcal{F}_{\alpha\beta} m_q \\ &- 96\alpha\beta (\alpha + \beta) m_c m_q^2 + m_c \mathcal{F}_{\alpha\beta} (\alpha + \beta - 1) (94\alpha + 94\beta + 1)), \end{aligned} \quad (A5)$$

$$\begin{aligned} \rho_{0^{++},A}^{\langle \bar{q}q \rangle^2}(s) &= \frac{\langle \bar{q}q \rangle^2}{\pi^4} \int_{\alpha_{min}}^{\alpha_{max}} d\alpha \left\{ \int_{\beta_{min}}^{1-\alpha} d\beta \left[-\frac{g_s^2 m_c m_q \mathcal{F}_{\alpha\beta}^2 (\alpha + \beta)}{3 \times 2^5 \alpha^2 \beta^2} \right] \right. \\ &+ \left. \left[\frac{g_s^2 \mathcal{H}_\alpha^2 m_q^2}{3 \times 2^5 \alpha (\alpha - 1)} \right] \right\}, \end{aligned} \quad (A6)$$

$$\begin{aligned} \rho_{0^{++},A}^{\langle G^3 \rangle, I}(s) &= \frac{\langle g_s^3 G^3 \rangle}{\pi^6} \int_{\alpha_{min}}^{\alpha_{max}} d\alpha \int_{\beta_{min}}^{1-\alpha} d\beta - \frac{\mathcal{F}_{\alpha\beta}}{3 \times 2^{11} \alpha^3 \beta^3} [2\alpha\beta \mathcal{F}_{\alpha\beta}^2 - 12\alpha\beta m_q^2 m_c^2 (\alpha^2 - \beta^2 \\ &- \alpha\beta + \beta - \alpha) - 3m_c \mathcal{F}_{\alpha\beta} (\alpha m_q (\alpha^2 - \beta^2 - 3\alpha\beta + \beta - \alpha) + \beta m_q (\alpha^2 - \beta^2 \\ &- \alpha\beta + \beta - \alpha))] , \end{aligned} \quad (A7)$$

$$\begin{aligned} \rho_{0^{++},A}^{\langle G^3 \rangle, II}(s) &= \frac{\langle g_s^3 G^3 \rangle}{\pi^8} \int_{\alpha_{min}}^{\alpha_{max}} d\alpha \int_{\beta_{min}}^{1-\alpha} d\beta \frac{g_s^2 \mathcal{F}_{\alpha\beta} (\alpha + \beta - 1)^3}{3^3 \times 2^{14} \alpha^5 \beta^5} [2\mathcal{F}_{\alpha\beta}^2 (\alpha^3 + \beta^3) \\ &+ 12m_c^3 m_q (\alpha + \beta) (\alpha^4 + \beta^4) + 3m_c \mathcal{F}_{\alpha\beta} (6\alpha^4 m_q + 6\beta^4 m_q \\ &+ \alpha\beta m_q (\alpha^2 + \beta^2) + 4m_c (\alpha^4 + \beta^4))] , \end{aligned} \quad (A8)$$

$$\rho_{0^{++},A}^{\langle \bar{q}q \rangle \langle \bar{q}Gq \rangle}(s) = \frac{g_s^2 \langle \bar{q}q \rangle \langle g_s \bar{q} \sigma \cdot Gq \rangle}{\pi^4} \int_{\alpha_{min}}^{\alpha_{max}} d\alpha \left\{ \int_{\beta_{min}}^{1-\alpha} d\beta \left[-\frac{m_c m_q \mathcal{F}_{\alpha\beta}}{3^2 \times 2^{11} \alpha \beta} \right] \right.$$

$$\begin{aligned}
& + \frac{1}{3^2 \times 2^6 \alpha (\alpha - 1)} \left[-12\mathcal{H}_\alpha \alpha (\alpha - 1) m_q^2 + 4\alpha (\alpha - 1) m_c^2 m_q^2 \right. \\
& \left. + 5m_c \mathcal{H}_\alpha m_q \right] \Big\}, \tag{A9}
\end{aligned}$$

where, the subscript *I* and *II* for the gluon condensate come from dynamic gluon and quarks, respectively. Here,

$$\mathcal{F}_{\alpha\beta} = (\alpha + \beta) m_c^2 - \alpha\beta s, \mathcal{H}_\alpha = m_c^2 - \alpha(1 - \alpha)s, \tag{A10}$$

$$\alpha_{min} = \left(1 - \sqrt{1 - 4m_c^2/s}\right) / 2, \alpha_{max} = \left(1 + \sqrt{1 - 4m_c^2/s}\right) / 2, \tag{A11}$$

$$\beta_{min} = \alpha m_c^2 / (s\alpha - m_c^2). \tag{A12}$$

For the current shown in Eq. (4), we obtain the spectral densities as follows:

$$\rho_{0^{++},B}^{pert}(s) = \int_{\alpha_{min}}^{\alpha_{max}} d\alpha \int_{\beta_{min}}^{1-\alpha} d\beta \frac{g_s^2 \mathcal{F}_{\alpha\beta}^5 (\alpha + \beta - 1)^3 (\mathcal{F}_{\alpha\beta} - 3m_c m_q (\alpha + \beta))}{5 \times 3^2 \times 2^{11} \pi^8 \alpha^5 \beta^5}, \tag{A13}$$

$$\begin{aligned}
\rho_{0^{++},B}^{\langle \bar{q}q \rangle}(s) &= \frac{\langle \bar{q}q \rangle}{\pi^6} \int_{\alpha_{min}}^{\alpha_{max}} d\alpha \int_{\beta_{min}}^{1-\alpha} d\beta \frac{g_s^2 \mathcal{F}_{\alpha\beta}^3 (\alpha + \beta - 1)}{3 \times 2^9 \alpha^4 \beta^4} (4\alpha\beta \mathcal{F}_{\alpha\beta} m_q \\
&- 4\alpha\beta m_c m_q^2 (\alpha + \beta) + m_c \mathcal{F}_{\alpha\beta} (\alpha + \beta) (\alpha + \beta - 1)), \tag{A14}
\end{aligned}$$

$$\begin{aligned}
\rho_{0^{++},B}^{\langle G^2 \rangle, I}(s) &= \frac{\langle g_s^2 G^2 \rangle}{\pi^6} \int_{\alpha_{min}}^{\alpha_{max}} d\alpha \int_{\beta_{min}}^{1-\alpha} d\beta - \frac{m_c \mathcal{F}_{\alpha\beta}^2 (\alpha + \beta - 1)}{3 \times 2^9 \alpha^3 \beta^3} (\mathcal{F}_{\alpha\beta} m_q (\alpha \\
&+ \beta) - 6\alpha\beta m_c m_q^2), \tag{A15}
\end{aligned}$$

$$\begin{aligned}
\rho_{0^{++},B}^{\langle G^2 \rangle, II}(s) &= \frac{g_s^2 \langle g_s^2 G^2 \rangle}{\pi^8} \int_{\alpha_{min}}^{\alpha_{max}} d\alpha \int_{\beta_{min}}^{1-\alpha} d\beta \left(- \frac{m_c \mathcal{F}_{\alpha\beta}^2 (\alpha + \beta - 1)^3}{3^3 \times 2^{12} \alpha^5 \beta^5} (\alpha^3 \mathcal{F}_{\alpha\beta} (3m_q \right. \\
&- 2m_c) + \beta^3 \mathcal{F}_{\alpha\beta} (3m_q - 2m_c) + 3m_c^2 m_q (\alpha^3 + \beta^3) (\alpha + \beta) \\
&+ \frac{\mathcal{F}_{\alpha\beta}^3 (\alpha + \beta - 1)}{3^3 \times 2^{19} \alpha^4 \beta^4} (-\mathcal{F}_{\alpha\beta} (1 - 5\alpha + 4\alpha^2 - 5\beta + 4\beta^2 + 14\alpha\beta) \\
&+ 4m_c (\alpha + \beta - 1) (\beta m_q (49\alpha + 4\beta - 1) + \alpha m_q (49\beta + 4\alpha - 1))) \Big), \tag{A16}
\end{aligned}$$

$$\begin{aligned}
\rho_{0^{++},B}^{\langle \bar{q}Gq \rangle}(s) &= - \frac{\langle g_s \bar{q} \sigma \cdot Gq \rangle}{\pi^6} \int_{\alpha_{min}}^{\alpha_{max}} d\alpha \int_{\beta_{min}}^{1-\alpha} d\beta \frac{g_s^2 \mathcal{F}_{\alpha\beta}^2}{3^2 \times 2^{13} \alpha^3 \beta^3} (128m_q \alpha \beta \mathcal{F}_{\alpha\beta} \\
&- 96\alpha\beta (\alpha + \beta) m_c m_q^2 + m_c \mathcal{F}_{\alpha\beta} (\alpha + \beta - 1) (94\alpha + 94\beta + 1)), \tag{A17}
\end{aligned}$$

$$\begin{aligned}
\rho_{0^{++},B}^{\langle \bar{q}q \rangle^2}(s) &= \frac{\langle \bar{q}q \rangle^2}{\pi^4} \int_{\alpha_{min}}^{\alpha_{max}} d\alpha \left\{ \int_{\beta_{min}}^{1-\alpha} d\beta \left[\frac{g_s^2 m_c \mathcal{F}_{\alpha\beta}^2 m_q (\alpha + \beta)}{3 \times 2^5 \alpha^2 \beta^2} \right] \right. \\
&+ \left. \left[\frac{g_s^2 \mathcal{H}_\alpha^2 m_q^2}{3 \times 2^5 \alpha (\alpha - 1)} \right] \right\}, \tag{A18}
\end{aligned}$$

$$\begin{aligned}
\rho_{0^{++},B}^{\langle G^3 \rangle, I}(s) &= \frac{\langle g_s^3 G^3 \rangle}{\pi^6} \int_{\alpha_{min}}^{\alpha_{max}} d\alpha \int_{\beta_{min}}^{1-\alpha} d\beta - \frac{\mathcal{F}_{\alpha\beta}}{3 \times 2^{11} \alpha^3 \beta^3} [2\alpha\beta \mathcal{F}_{\alpha\beta}^2 \\
&- 12\alpha\beta m_q^2 m_c^2 (\alpha^2 - \beta^2 - \alpha\beta + \beta - \alpha) + 3m_c \mathcal{F}_{\alpha\beta} (\alpha m_q (\alpha^2 - \beta^2)
\end{aligned}$$

$$- 3\alpha\beta + \beta - \alpha) + \beta m_q(\alpha^2 - \beta^2 - \alpha\beta + \beta - \alpha)] , \quad (\text{A19})$$

$$\begin{aligned} \rho_{0^{++},B}^{\langle G^3 \rangle,II}(s) &= \frac{\langle g_s^3 G^3 \rangle}{\pi^8} \int_{\alpha_{min}}^{\alpha_{max}} d\alpha \int_{\beta_{min}}^{1-\alpha} d\beta - \frac{g_s^2 \mathcal{F}_{\alpha\beta}(\alpha + \beta - 1)^3}{3^3 \times 2^{14} \alpha^5 \beta^5} [-2\mathcal{F}_{\alpha\beta}^2(\alpha^3 + \beta^3) \\ &+ 12m_c^3 m_q(\alpha + \beta)(\alpha^4 + \beta^4) + 3m_c \mathcal{F}_{\alpha\beta}(6\alpha^4 m_q + 6\beta^4 m_q \\ &+ m_q \alpha\beta(\alpha^2 + \beta^2) - 4m_c(\alpha^4 + \beta^4))] , \end{aligned} \quad (\text{A20})$$

$$\begin{aligned} \rho_{0^+,B}^{\langle \bar{q}q \rangle \langle \bar{q}Gq \rangle}(s) &= \frac{g_s^2 \langle \bar{q}q \rangle \langle g_s \bar{q}\sigma \cdot Gq \rangle}{\pi^4} \int_{\alpha_{min}}^{\alpha_{max}} d\alpha \left\{ \int_{\beta_{min}}^{1-\alpha} d\beta \left[\frac{m_c \mathcal{F}_{\alpha\beta} m_q}{3^2 \times 2^{10} \alpha \beta} \right] \right. \\ &+ \frac{1}{3^2 \times 2^6 \alpha(\alpha - 1)} [-12\mathcal{H}_\alpha \alpha(\alpha - 1)m_q^2 + 4\alpha(\alpha - 1)m_c^2 m_q^2 \\ &\left. - 5m_c \mathcal{H}_\alpha m_q \right\} . \end{aligned} \quad (\text{A21})$$

For the current showed in Eq. (5), we obtain the spectral densities as follows:

$$\rho_{0^{++},C}^{pert}(s) = \int_{\alpha_{min}}^{\alpha_{max}} d\alpha \int_{\beta_{min}}^{1-\alpha} d\beta \frac{g_s^2 \mathcal{F}_{\alpha\beta}^6(\alpha + \beta - 1)^3}{5 \times 3^2 \times 2^{11} \pi^8 \alpha^5 \beta^5} , \quad (\text{A22})$$

$$\rho_{0^{++},C}^{\langle \bar{q}q \rangle}(s) = \frac{\langle \bar{q}q \rangle}{\pi^6} \int_{\alpha_{min}}^{\alpha_{max}} d\alpha \int_{\beta_{min}}^{1-\alpha} d\beta \frac{g_s^2 m_q \mathcal{F}_{\alpha\beta}^4(\alpha + \beta - 1)}{3 \times 2^7 \alpha^3 \beta^3} , \quad (\text{A23})$$

$$\rho_{0^{++},C}^{\langle G^2 \rangle,I}(s) = \frac{\langle g_s^2 G^2 \rangle}{\pi^6} \int_{\alpha_{min}}^{\alpha_{max}} d\alpha \int_{\beta_{min}}^{1-\alpha} d\beta \frac{m_c^2 m_q^2 \mathcal{F}_{\alpha\beta}^2(\alpha + \beta - 1)}{2^8 \alpha^2 \beta^2} , \quad (\text{A24})$$

$$\begin{aligned} \rho_{0^{++},C}^{\langle G^2 \rangle,II}(s) &= \frac{g_s^2 \langle g_s^2 G^2 \rangle}{\pi^8} \int_{\alpha_{min}}^{\alpha_{max}} d\alpha \int_{\beta_{min}}^{1-\alpha} d\beta \left(\frac{m_c^2 \mathcal{F}_{\alpha\beta}^3(\alpha + \beta - 1)^3(\alpha^3 + \beta^3)}{3^3 \times 2^{11} \alpha^5 \beta^5} \right. \\ &\left. + \frac{\mathcal{F}_{\alpha\beta}^4(\alpha + \beta - 1)(\alpha + \beta)}{3^2 \times 2^{18} \alpha^4 \beta^4} \right) , \end{aligned} \quad (\text{A25})$$

$$\rho_{0^{++},C}^{\langle \bar{q}Gq \rangle}(s) = -\frac{\langle g_s \bar{q}\sigma \cdot Gq \rangle}{\pi^6} \int_{\alpha_{min}}^{\alpha_{max}} d\alpha \int_{\beta_{min}}^{1-\alpha} d\beta \frac{g_s^2 m_q \mathcal{F}_{\alpha\beta}^3}{3^2 \times 2^6 \alpha^2 \beta^2} , \quad (\text{A26})$$

$$\rho_{0^{++},C}^{\langle \bar{q}q \rangle^2}(s) = \frac{\langle \bar{q}q \rangle^2}{\pi^4} \int_{\alpha_{min}}^{\alpha_{max}} d\alpha \left\{ \frac{g_s^2 \mathcal{H}_\alpha^2 m_q^2}{3 \times 2^5 \alpha(\alpha - 1)} \right\} , \quad (\text{A27})$$

$$\begin{aligned} \rho_{0^{++},C}^{\langle G^3 \rangle,I}(s) &= \frac{\langle g_s^3 G^3 \rangle}{\pi^6} \int_{\alpha_{min}}^{\alpha_{max}} d\alpha \int_{\beta_{min}}^{1-\alpha} d\beta - \frac{1}{3 \times 2^{10} \alpha^2 \beta^2} [\mathcal{F}_{\alpha\beta}^3 \\ &+ 6m_q^2 m_c^2 \mathcal{F}_{\alpha\beta}(-4\alpha^2 + 4\beta^2 + \alpha\beta - 4\beta + 4\alpha)] , \end{aligned} \quad (\text{A28})$$

$$\begin{aligned} \rho_{0^{++},C}^{\langle G^3 \rangle,II}(s) &= \frac{\langle g_s^3 G^3 \rangle}{\pi^8} \int_{\alpha_{min}}^{\alpha_{max}} d\alpha \int_{\beta_{min}}^{1-\alpha} d\beta \frac{g_s^2 \mathcal{F}_{\alpha\beta}^2(\alpha + \beta - 1)^3}{3^3 \times 2^{13} \alpha^5 \beta^5} [\mathcal{F}_{\alpha\beta}(\alpha^3 + \beta^3) \\ &+ 6m_c^2(\alpha^4 + \beta^4)] , \end{aligned} \quad (\text{A29})$$

$$\rho_{0^{++},C}^{\langle \bar{q}q \rangle \langle \bar{q}Gq \rangle}(s) = \frac{g_s^2 \langle \bar{q}q \rangle \langle g_s \bar{q}\sigma \cdot Gq \rangle}{\pi^4} \int_{\alpha_{min}}^{\alpha_{max}} d\alpha \left\{ \frac{(m_c^2 - 3\mathcal{H}_\alpha)m_q^2}{3^2 \times 2^4} \right\} . \quad (\text{A30})$$

2. The spectral densities for 0^{-+} gluonic tetraquark states

For the current shown in Eq. (6), we obtain the spectral densities as follows:

$$\rho_{0^{-+},A}^{pert}(s) = \rho_{0^{++},A}^{pert}(s), \quad (\text{A31})$$

$$\rho_{0^{-+},A}^{\langle \bar{q}q \rangle}(s) = \rho_{0^{++},A}^{\langle \bar{q}q \rangle}(s), \quad (\text{A32})$$

$$\rho_{0^{-+},A}^{\langle G^2 \rangle, I}(s) = -\rho_{0^{++},A}^{\langle G^2 \rangle, I}(s), \quad (\text{A33})$$

$$\rho_{0^{-+},A}^{\langle G^2 \rangle, II}(s) = \rho_{0^{++},A}^{\langle G^2 \rangle, II}(s), \quad (\text{A34})$$

$$\rho_{0^{-+},A}^{\langle \bar{q}Gq \rangle}(s) = \rho_{0^{++},A}^{\langle \bar{q}Gq \rangle}(s), \quad (\text{A35})$$

$$\rho_{0^{-+},A}^{\langle \bar{q}q \rangle^2}(s) = \rho_{0^{++},A}^{\langle \bar{q}q \rangle^2}(s), \quad (\text{A36})$$

$$\begin{aligned} \rho_{0^{-+},A}^{\langle G^3 \rangle, I}(s) &= \frac{\langle g_s^3 G^3 \rangle}{\pi^6} \int_{\alpha_{min}}^{\alpha_{max}} d\alpha \int_{\beta_{min}}^{1-\alpha} d\beta - \frac{\mathcal{F}_{\alpha\beta}}{3 \times 2^{10} \alpha^3 \beta^3} [\alpha\beta \mathcal{F}_{\alpha\beta}^2 \\ &+ 6\alpha\beta m_q^2 m_c^2 (4\alpha^2 - 4\beta^2 - \alpha\beta + \beta - \alpha) + 6m_c \mathcal{F}_{\alpha\beta} (\alpha m_q (\alpha^2 \\ &- \beta^2 - \alpha\beta + \beta - \alpha) + \beta m_q (\alpha^2 - \beta^2 + \alpha\beta + \beta - \alpha))] , \end{aligned} \quad (\text{A37})$$

$$\rho_{0^{-+},A}^{\langle G^3 \rangle, II}(s) = \rho_{0^{++},A}^{\langle G^3 \rangle, II}(s), \quad (\text{A38})$$

$$\rho_{0^{-+},A}^{\langle \bar{q}q \rangle \langle \bar{q}Gq \rangle}(s) = \rho_{0^{++},A}^{\langle \bar{q}q \rangle \langle \bar{q}Gq \rangle}(s). \quad (\text{A39})$$

For the currents shown in Eq. (7), we obtain the spectral densities as follows:

$$\rho_{0^{-+},B}^{pert}(s) = \rho_{0^{++},B}^{pert}(s), \quad (\text{A40})$$

$$\rho_{0^{-+},B}^{\langle \bar{q}q \rangle}(s) = \rho_{0^{++},B}^{\langle \bar{q}q \rangle}(s), \quad (\text{A41})$$

$$\rho_{0^{-+},B}^{\langle G^2 \rangle, I}(s) = -\rho_{0^{++},B}^{\langle G^2 \rangle, I}(s), \quad (\text{A42})$$

$$\rho_{0^{-+},B}^{\langle G^2 \rangle, II}(s) = \rho_{0^{++},B}^{\langle G^2 \rangle, II}(s), \quad (\text{A43})$$

$$\rho_{0^{-+},B}^{\langle \bar{q}Gq \rangle}(s) = \rho_{0^{++},B}^{\langle \bar{q}Gq \rangle}(s), \quad (\text{A44})$$

$$\rho_{0^{-+},B}^{\langle \bar{q}q \rangle^2}(s) = \rho_{0^{++},B}^{\langle \bar{q}q \rangle^2}(s), \quad (\text{A45})$$

$$\begin{aligned} \rho_{0^{-+},B}^{\langle G^3 \rangle, I}(s) &= \frac{\langle g_s^3 G^3 \rangle}{\pi^6} \int_{\alpha_{min}}^{\alpha_{max}} d\alpha \int_{\beta_{min}}^{1-\alpha} d\beta - \frac{\mathcal{F}_{\alpha\beta}}{3 \times 2^{10} \alpha^3 \beta^3} [\alpha\beta \mathcal{F}_{\alpha\beta}^2 + 6\alpha\beta m_q^2 m_c^2 (4\alpha^2 - 4\beta^2 \\ &- \alpha\beta + 4\beta - 4\alpha) - 6m_c \mathcal{F}_{\alpha\beta} (\alpha m_q (\alpha^2 - \beta^2 - \alpha\beta + \beta - \alpha) + \beta m_q (\alpha^2 - \beta^2 \\ &+ \alpha\beta + \beta - \alpha))] , \end{aligned} \quad (\text{A46})$$

$$\rho_{0^{-+},B}^{\langle G^3 \rangle, II}(s) = \rho_{0^{++},B}^{\langle G^3 \rangle, II}(s), \quad (\text{A47})$$

$$\rho_{0^{-+},B}^{\langle \bar{q}q \rangle \langle \bar{q}Gq \rangle}(s) = \rho_{0^{++},B}^{\langle \bar{q}q \rangle \langle \bar{q}Gq \rangle}(s). \quad (\text{A48})$$

For the current shown in Eq. (8), we obtain the spectral densities as follows:

$$\rho_{0^{-+},C}^{pert}(s) = \rho_{0^{++},C}^{pert}(s), \quad (\text{A49})$$

$$\rho_{0^{-+},C}^{\langle \bar{q}q \rangle}(s) = \rho_{0^{++},C}^{\langle \bar{q}q \rangle}(s), \quad (\text{A50})$$

$$\rho_{0^{-+},C}^{\langle G^2 \rangle, I}(s) = -\rho_{0^{++},C}^{\langle G^2 \rangle, I}(s), \quad (\text{A51})$$

$$\rho_{0^{-+},C}^{\langle G^2 \rangle, II}(s) = \rho_{0^{++},C}^{\langle G^2 \rangle, II}(s), \quad (\text{A52})$$

$$\rho_{0^{-+},C}^{\langle \bar{q}Gq \rangle}(s) = \rho_{0^{++},C}^{\langle \bar{q}Gq \rangle}(s), \quad (\text{A53})$$

$$\rho_{0^{-+},C}^{\langle \bar{q}q \rangle^2}(s) = \rho_{0^{++},C}^{\langle \bar{q}q \rangle^2}(s), \quad (\text{A54})$$

$$\begin{aligned} \rho_{0^{-+},C}^{\langle G^3 \rangle, I}(s) &= \frac{\langle g_s^3 G^3 \rangle}{\pi^6} \int_{\alpha_{min}}^{\alpha_{max}} d\alpha \int_{\beta_{min}}^{1-\alpha} d\beta - \frac{1}{3 \times 2^{10} \alpha^2 \beta^2} [\mathcal{F}_{\alpha\beta}^3 \\ &+ 6m_q^2 m_c^2 \mathcal{F}_{\alpha\beta}(\alpha^2 - \beta^2 - \alpha\beta + \beta - \alpha)], \end{aligned} \quad (\text{A55})$$

$$\rho_{0^{-+},C}^{\langle G^3 \rangle, II}(s) = \rho_{0^{++},C}^{\langle G^3 \rangle, II}(s), \quad (\text{A56})$$

$$\rho_{0^{-+},C}^{\langle \bar{q}q \rangle \langle \bar{q}Gq \rangle}(s) = \rho_{0^{++},C}^{\langle \bar{q}q \rangle \langle \bar{q}Gq \rangle}(s). \quad (\text{A57})$$

3. The spectral densities for 0^{--} gluonic tetraquark states

For the current shown in Eq. (10), we obtain the spectral densities as follows:

$$\rho_{0^{--},A}^{pert}(s) = \rho_{0^{-+},C}^{pert}(s), \quad (\text{A58})$$

$$\rho_{0^{--},A}^{\langle \bar{q}q \rangle}(s) = \rho_{0^{-+},C}^{\langle \bar{q}q \rangle}(s), \quad (\text{A59})$$

$$\rho_{0^{--},A}^{\langle G^2 \rangle, I}(s) = \rho_{0^{-+},C}^{\langle G^2 \rangle, I}(s), \quad (\text{A60})$$

$$\begin{aligned} \rho_{0^{--},A}^{\langle G^2 \rangle, II}(s) &= \frac{g_s^2 \langle g_s^2 G^2 \rangle}{\pi^8} \int_{\alpha_{min}}^{\alpha_{max}} d\alpha \int_{\beta_{min}}^{1-\alpha} d\beta \left(\frac{m_c^2 \mathcal{F}_{\alpha\beta}^3 (\alpha + \beta - 1)^3 (\alpha^3 + \beta^3)}{3^3 \times 2^{11} \alpha^5 \beta^5} \right. \\ &+ \left. \frac{\mathcal{F}_{\alpha\beta}^4 (\alpha + \beta - 1)(\alpha^2 + (\beta - 1)^2 - 2\alpha + 8\alpha\beta)}{3^3 \times 2^{18} \alpha^4 \beta^4} \right), \end{aligned} \quad (\text{A61})$$

$$\rho_{0^{--},A}^{\langle \bar{q}Gq \rangle}(s) = \rho_{0^{-+},C}^{\langle \bar{q}Gq \rangle}(s), \quad (\text{A62})$$

$$\rho_{0^{--},A}^{\langle \bar{q}q \rangle^2}(s) = \rho_{0^{-+},C}^{\langle \bar{q}q \rangle^2}(s), \quad (\text{A63})$$

$$\rho_{0^{--},A}^{\langle G^3 \rangle, I}(s) = \rho_{0^{-+},C}^{\langle G^3 \rangle, I}(s), \quad (\text{A64})$$

$$\rho_{0^{--},A}^{\langle G^3 \rangle, II}(s) = \rho_{0^{-+},C}^{\langle G^3 \rangle, II}(s), \quad (\text{A65})$$

$$\rho_{0^{--},A}^{\langle \bar{q}q \rangle \langle \bar{q}Gq \rangle}(s) = \rho_{0^{-+},C}^{\langle \bar{q}q \rangle \langle \bar{q}Gq \rangle}(s). \quad (\text{A66})$$

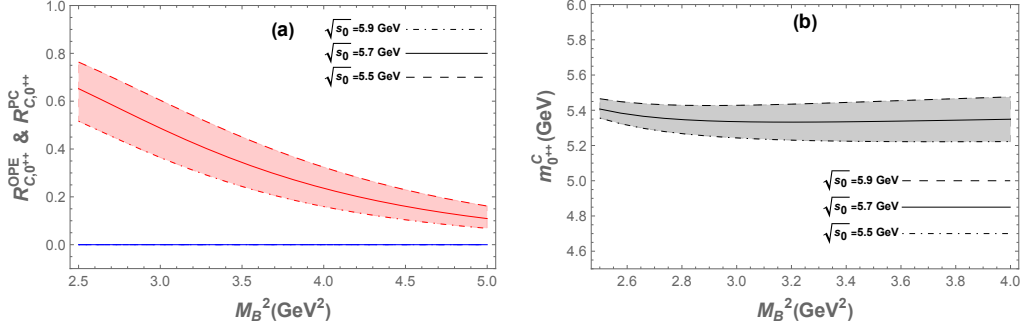


FIG. 3: Similar captions as in Fig. 2, but for the current in Eq. (5).

For the currents shown in Eq. (10), we obtain the spectral densities as follows:

$$\rho_{0^{+-},A}^{pert}(s) = \rho_{0^{--},A}^{pert}(s), \quad (\text{A67})$$

$$\rho_{0^{+-},A}^{\langle \bar{q}q \rangle}(s) = \rho_{0^{--},A}^{\langle \bar{q}q \rangle}(s), \quad (\text{A68})$$

$$\rho_{0^{+-},A}^{\langle G^2 \rangle, I}(s) = -\rho_{0^{--},A}^{\langle G^2 \rangle, I}(s), \quad (\text{A69})$$

$$\rho_{0^{+-},A}^{\langle G^2 \rangle, II}(s) = \rho_{0^{--},A}^{\langle G^2 \rangle, II}(s), \quad (\text{A70})$$

$$\rho_{0^{+-},A}^{\langle \bar{q}Gq \rangle}(s) = \rho_{0^{--},A}^{\langle \bar{q}Gq \rangle}(s), \quad (\text{A71})$$

$$\rho_{0^{+-},A}^{\langle \bar{q}q \rangle^2}(s) = \rho_{0^{--},A}^{\langle \bar{q}q \rangle^2}(s), \quad (\text{A72})$$

$$\rho_{0^{+-},B}^{\langle G^3 \rangle, I}(s) = \frac{\langle g_s^3 G^3 \rangle}{\pi^6} \int_{\alpha_{min}}^{\alpha_{max}} d\alpha \int_{\beta_{min}}^{1-\alpha} d\beta - \frac{1}{3 \times 2^{10} \alpha^2 \beta^2} [\mathcal{F}_{\alpha\beta}^3 + 6m_q^2 m_c^2 \mathcal{F}_{\alpha\beta}(-4\alpha^2 + 4\beta^2 + \alpha\beta - \beta + 4\alpha)], \quad (\text{A73})$$

$$\rho_{0^{+-},A}^{\langle G^3 \rangle, II}(s) = \rho_{0^{--},A}^{\langle G^3 \rangle, II}(s), \quad (\text{A74})$$

$$\rho_{0^{+-},A}^{\langle \bar{q}q \rangle \langle \bar{q}Gq \rangle}(s) = \rho_{0^{--},A}^{\langle \bar{q}q \rangle \langle \bar{q}Gq \rangle}(s). \quad (\text{A75})$$

Appendix B: The ratios R^{OPE} , R^{PC} , and the masses m are plotted as functions of Borel parameter M_B^2

We display the figures of the R^{OPE} , R^{PC} , and the masses m as functions of Borel parameter M_B^2 for hidden-charm and -bottom tetraquark hybrid states below. It should be noted that the differences between the numerical results for $j_{0^+}^C$ and $j_{0^+}^D$ are so tiny that we just plot the case of $j_{0^+}^C$. The same applies to the pairs $(j_{0^-}^C, j_{0^-}^D)$, $(j_{1^-}^B, j_{1^-}^F)$, $(j_{1^-}^C, j_{1^-}^G)$, and $(j_{1^+}^C, j_{1^+}^G)$.

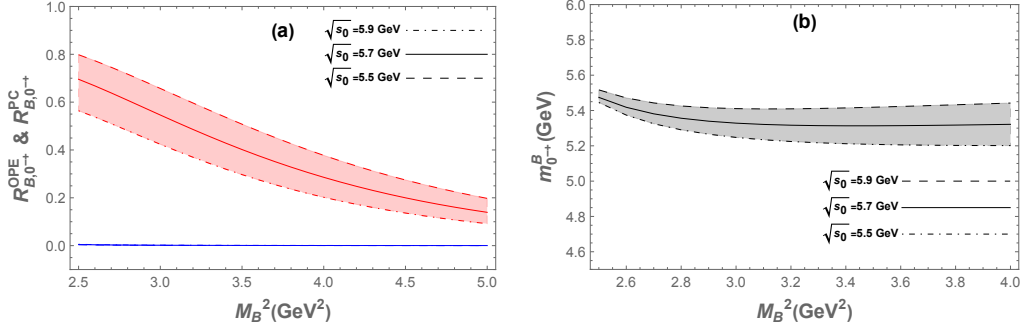


FIG. 4: Similar captions as in Fig. 2, but for the current in Eq. (7).

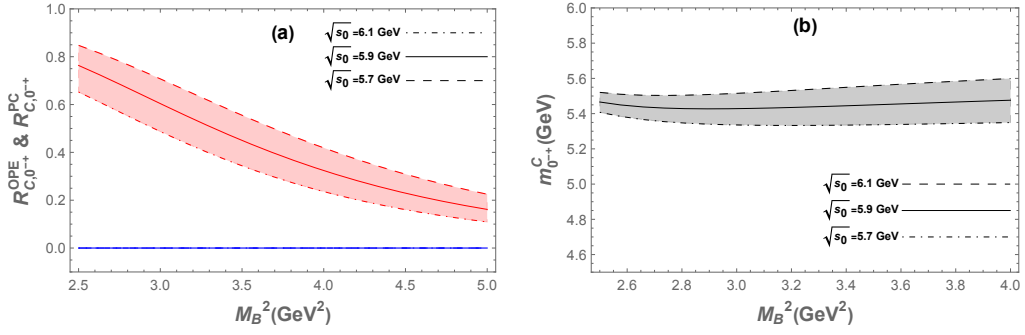


FIG. 5: Similar captions as in Fig. 2, but for the current in Eq. (8).

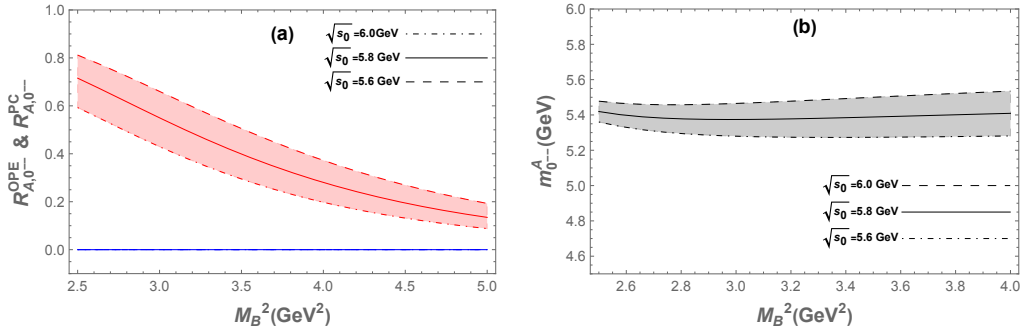


FIG. 6: Similar captions as in Fig. 2, but for the current in Eq. (10)

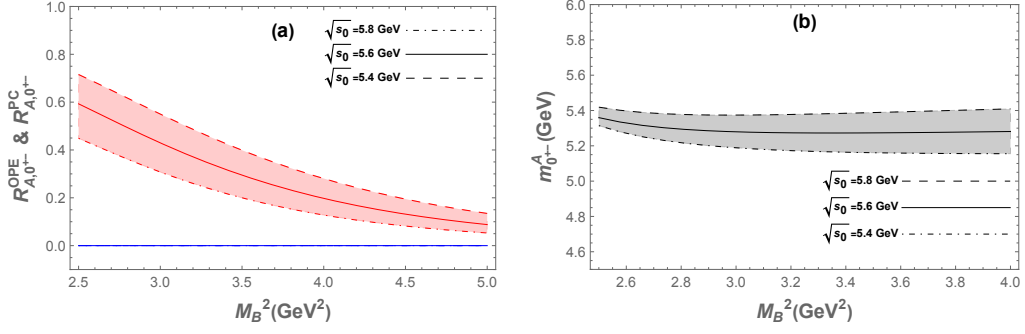


FIG. 7: Similar captions as in Fig. 2, but for the current in Eq. (10).

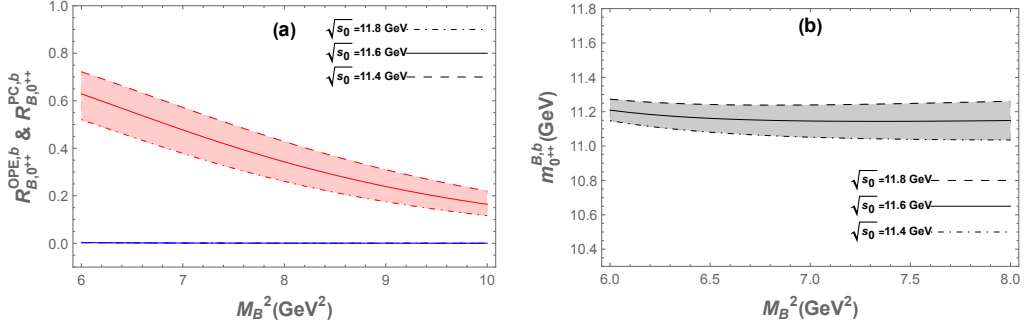


FIG. 8: Similar captions as in Fig. 2, but for the b -sector and for the current in Eq. (4).

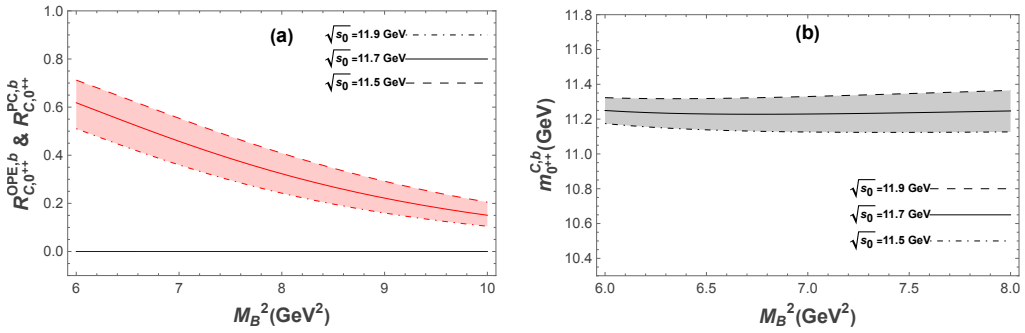


FIG. 9: Similar captions as in Fig. 2, but for the b -sector and for the current in Eq. (5).

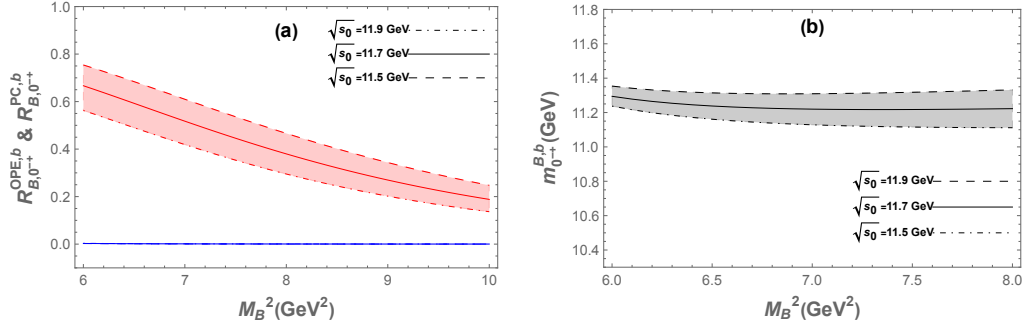


FIG. 10: Similar captions as in Fig. 2, but for the b -sector and for the current in Eq. (7).

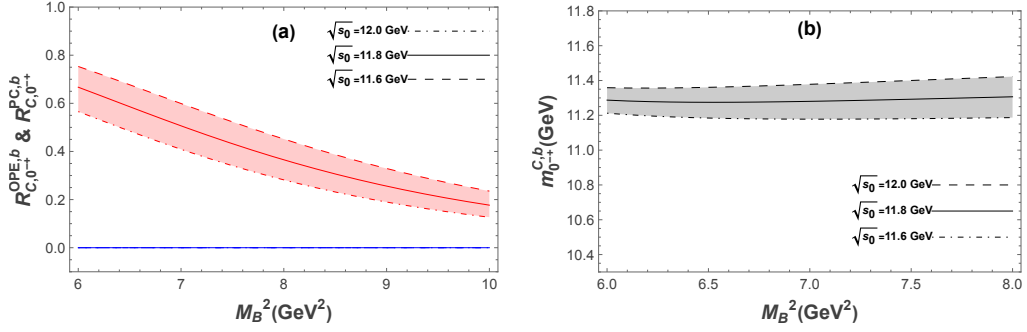


FIG. 11: Similar captions as in Fig. 2, but for the b -sector and for the current in Eq. (8).

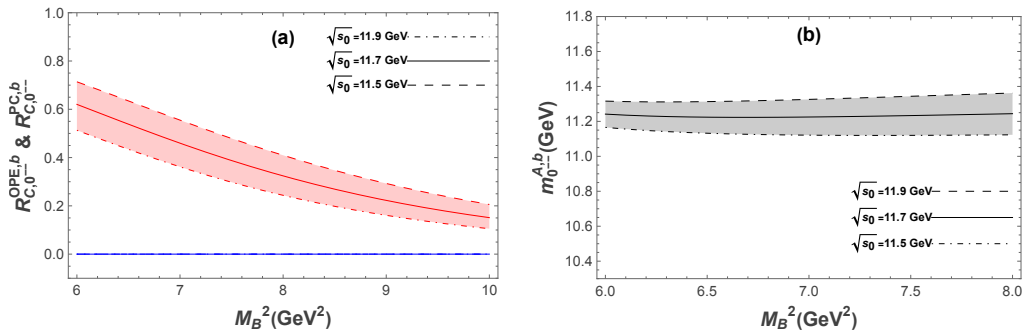


FIG. 12: Similar captions as in Fig. 2, but for the b -sector and for the current in Eq. (10).

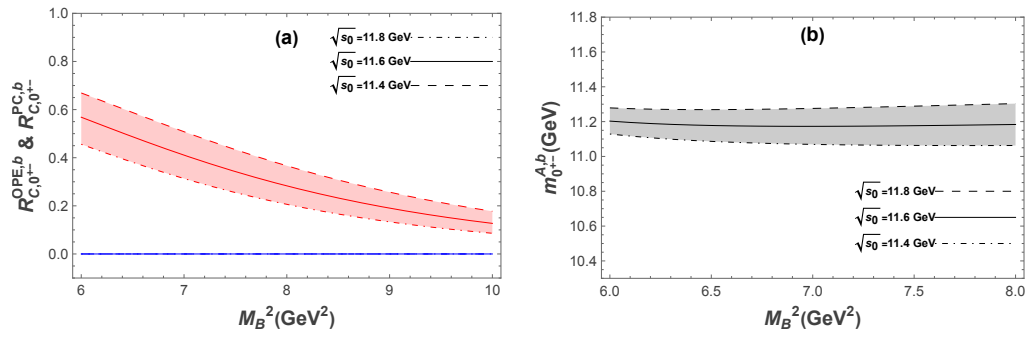


FIG. 13: Similar captions as in Fig. 2, but for the b -sector and for the current in Eq. (10).